In vitro degradation resistance of glucose and *L*-cysteine-bioinspired Schiff-base anodic Ca−P coating on AZ31 magnesium alloy

Xue-mei WANG[1], Xiao-li FAN[1], Mei-qi ZENG[1], Chang-yang LI[1],
Lan-yue CUI[1], Xiao-bo CHEN[2], Yu-hong ZOU[3], Zhen-lin WANG[4], Rong-chang ZENG[1,5]

1. Corrosion Laboratory for Light Metals, College of Materials Science and Engineering,
Shandong University of Science and Technology, Qingdao 266590, China;
2. School of Engineering, RMIT University, Carlton 3053, VIC, Australia;
3. School of Chemical and Biological Engineering,
Shandong University of Science and Technology, Qingdao 266590, China;
4. School of Materials Science and Engineering, Chongqing University of Technology, Chongqing 400054, China;
5. School of Materials Science and Engineering, Zhengzhou University, Zhengzhou 450002, China

Abstract: A Schiff base (a compound containing a C=N bond) induced anodic Ca−P coating was prepared on AZ31 Mg alloy in a mixed solution of $CaCl_2$ and KH_2PO_4 at 60 °C in the presence of glucose and *L*-cysteine. The microstructure and chemical composition of the coatings were characterized using FE-SEM, FT-IR, XRD, and XPS. The in vitro degradation resistance of the coated samples was evaluated via potentiodynamic polarization (PDP), electrochemical impedance spectroscopy (EIS), and hydrogen evolution test. The experimental results show that the Ca−P$_{Schiff base}$ coating is composed of $CaHPO_4$ (DCPA) and hydroxyapatite (HA), whereas HA is not present in the Ca−P coating. The Ca−P$_{Schiff base}$ coating thickness is about 2 times that of Ca−P coating (Ca−P coating: (9.13±4.20) μm and Ca−P$_{Schiff base}$: (18.13±5.78) μm). The corrosion current density of the Ca−P$_{Schiff base}$ coating is two orders of magnitude lower than that of the Ca−P coating. The formation mechanism of the Ca−P$_{Schiff base}$ is proposed.

Key words: magnesium alloy; anodic coating; corrosion resistance; Schiff base; biomaterial

1 Introduction

Magnesium (Mg) and its alloys, with density and elastic modulus similar to human bone and excellent biocompatibility, are regarded as an ideal biodegradable metallic biomaterial [1−4]. However, the low potential and high chemical activity of Mg alloys may result in the clinic pre-failure [5−7] during the service period due to their high degradation rates.

It is well-known that calcium−phosphate (Ca−P) coatings can improve the degradation resistance of Mg alloys [8−12]. Ca−P can also stimulate bone regeneration and promote osseo-integration around implants. However, traditional Ca−P coating usually has poor adhesion [13] and coarse grains, resulting in higher porosity and limited degradation resistance. It has been reported that EDTA [14,15] and organic compounds, i.e. glucose [16], DNA [8], and amino acids [17] induced the formation of Ca−P coatings. For example, LI et al [16] prepared glucose-induced hydrothermal Ca−P coating on pure Mg. Compared with the traditional Ca−P coating, the glucose-induced Ca−P coating has refined grains, with an obviously reduced surface roughness. The results of the nanoscratch test showed that the adhesion of

glucose-induced Ca−P coating increased slightly. Also, DNA-induced Ca−P coating was prepared on AZ31 Mg alloy by LIU et al [8]. The grain size changed from micron level for the traditional Ca−P coating to nanometer level for the DNA-induced one, and as expected the surface roughness decreased. Notably, DNA-induced Ca−P coating exhibited a stronger binding with its substrate. Hence, it was concluded that organic additives significantly improved the compactness of Ca−P coatings.

Schiff base is the condensation product of an amine and a ketone or aldehyde and has the general formula R—C═N—R [18]. Studies have shown that the inhibition efficiency of Schiff base is significantly higher than that with the individual effect of amines and aldehydes, which has been attributed to the presence of imino group (C═N) in the molecular structure of Schiff base [19]. In fact, it is an effective corrosion inhibitor for steels in an acid medium, due to the presence of the —C═N group, electronegative N, S, and/or O atoms in the molecule [20]. STANLY JACOB et al [21] reported that Schiff base furoin thiosemicarbazone was used as a corrosion inhibitor of low carbon steels in hydrochloric acid solution. Results reveal it has a good inhibition effect, which increases with increasing concentration. The corrosion inhibition of Schiff base furoin thiosemicarbazone lies in the adsorption of organic molecules on the surface of low carbon steels. However, the organic molecular film adsorbed on the metal surface is too thin and uneven to play an inhibition effect in a short time with limited inhibition efficiency. However, LIN et al [18] prepared a layered double hydroxide (LDH) coating modified with Schiff base compounds, which was synthesized using vanillin and L-aspartic acid, on aluminum alloy by one-step in-situ synthesis at low temperature. The results show that the Schiff base is successfully inserted into the interlayer of layered double hydroxide, resulting in forming a smoother and denser coating. The modified coating also has excellent corrosion resistance. Therefore, it is realized that the unique molecular structure of the Schiff base compound can be utilized to modify the coating on metals to obtain a better physical and chemical performance.

At present, there are a few reports on Schiff base modified traditional Ca−P coatings on the surface of Mg alloys. The effect of Schiff base on the surface coating of Mg alloy has not been elucidated. In this work, firstly, the Schiff base was synthesized utilizing amino acid and glucose; secondly, the anode Ca−P coating was modified using Schiff base at 60 °C with water bath. The formation mechanism of the modified coating was discussed.

2 Experimental

2.1 Materials

In this work, AZ31Mg alloy was used as the base material. Prior to the coating process, alloy samples (dimensions: 20 mm × 20 mm × 5 mm) were polished with silicon-carbide paper (150# to 2500#) and washed with absolute ethanol, and then dried with warm air. The chemical reagents used for the coating, i.e., analytical grade calcium chloride ($CaCl_2$), potassium dihydrogen phosphate (KH_2PO_4), glucose, and L-cysteine were procured from Qingdao Jingke Chemical Reagent Co., Ltd., China.

2.2 Preparation of Schiff base solution

Firstly, 0.2 mol/L L-cysteine and glucose in the molar ratio of 1:1 were dissolved in deionized water, and then the pH was adjusted to 12−13 using 1 mol/L NaOH. Finally, the mixed solution was held at 120 °C for 2 h to obtain the Schiff base solution.

2.3 Preparation of coatings

Firstly, 0.25 mol/L $CaCl_2$ and KH_2PO_4 were dissolved in deionized water. Secondly, the polished sample was placed in the above Ca−P mixed solution at 60 °C for 30 min to obtain Ca−P coating; the polished sample was placed in the above Ca−P mixed solution containing 1 mmol/L Schiff base at 60 °C for 30 min to obtain anodic Ca−P$_{Schiff base}$ coating. A flow chart of the preparation of Ca−P and Ca−P$_{Schiff base}$ coatings is shown in Fig. 1.

2.4 Surface characterization

Scanning electron microscopy (SEM, Nova Nano SEM 450, FEI Corporation, USA) and energy dispersive spectroscopy (EDS) were used to analyze the surface morphology and element compositions of the samples. The thickness and element distribution of the coatings were determined by scanning the cross section of the
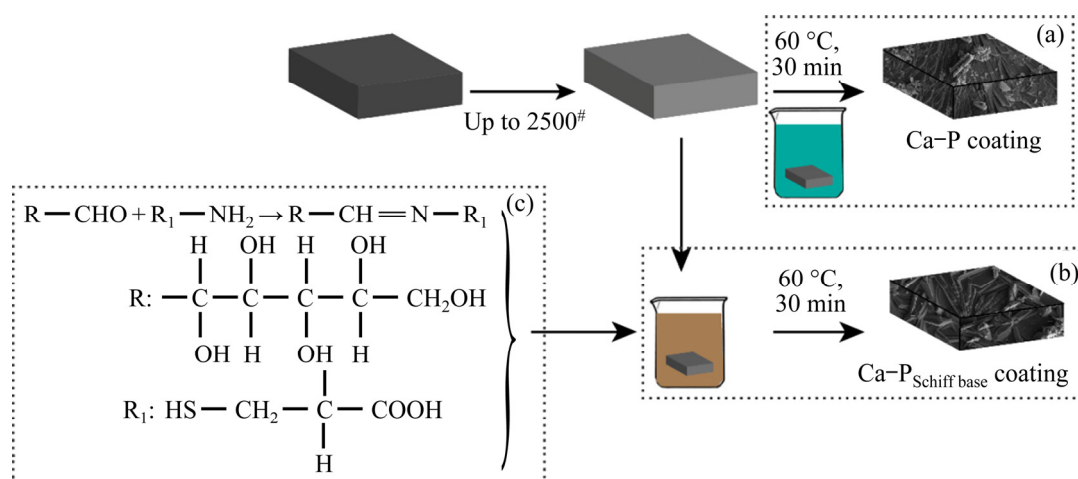
Fig. 1 Schematic illustration of preparation of Ca−P coating (a), anode Ca−P$_{\text{Schiff base}}$ coating (b), and Schiff base (c)

samples. Before SEM test, the sample surface was treated by vacuum gold plating. Crystallographic structure of the samples was detected through an X-ray diffractometer (Rigaku D/MAX2500PC, Japan) with a Cu target (λ=0.154 nm) from 5° to 80° over 2θ range at a scanning rate of 8 (°)/min. Chemical groups or bonds of the coatings were determined by Fourier transform infrared (FT-IR, Nicolet 380, Thermo Electron Corporation, US) in the wavenumber range from 4000 to 400 cm^{-1} with a resolution of 1 cm^{-1} and X-ray photoelectron spectrometer (XPS, ESCALAB250Xi, Thermo VG Co, East Sussex, US) with an Al K$_\alpha$ X-ray source. The surface roughness was evaluated by infinite focus microscopy (IFM, Zeta−20, USA).

The bond strength between the substrate and its coating was measured using WS−2500 coating adhesion automatic scratch tester (Micro Materials, Ltd.) with a Rockwell diamond probe (with a diameter of 90 μm). The tests were conducted at a scan rate of 2 mm/min by a linear increase in the load up to 20 N until the total scratch length reached 2 mm. The scratch images were photographed using an in-situ optical microscope system.

2.5 Corrosion tests

Electrochemical impedance spectroscopy (EIS) and potentiodynamic polarization (PDP) techniques were utilized to evaluate the corrosion resistance of the samples. The electrochemical techniques were performed using an electrochemical workstation (versa stat 4, Princeton, USA) with a typical three-electrode system. The sample with an exposed

area of 1 cm^2 was used as the working electrode, saturated calomel electrode as the reference electrode, and platinum electrode as the counter electrode. The experiments were carried out in Hank's solution at room temperature. After a relatively stable OCP was established (600 s), EIS test was carried out after a short delay of interference potential of 10 mV (vs SCE) in a frequency range from 100 kHz to 10 mHz, and EIS data were fitted with ZSimpWin software; PDP curves were recorded at a scanning rate of 2 mV/s, and electrochemical parameters of corrosion potential (φ_{corr}) and corrosion current density (J_{corr}) were fitted with the software of Versatudio and origin Pro 9.1. Finally, polarization resistance (R_{p}) is calculated by the Stern Geary equation (Eq. (1)):

$$R_{\text{p}}=\beta_a\beta_c/[2.303J_{\text{corr}}(\beta_a+\beta_c)] \tag{1}$$

The hydrogen evolution rate was measured by placing the sample in Hank's solution connected to a graduated burette at a temperature of (37.0±0.5) °C, and intermittently measuring the water level in the burette when the surface was completely exposed.

3 Results

3.1 Analysis of Schiff base

The FT-IR spectrum of Schiff base solution is shown in Fig. 2. The characteristic peak of —C═N appeared at 1594 cm^{-1} [22,23], indicating that the reaction of amino acid and glucose formed Schiff base [24].
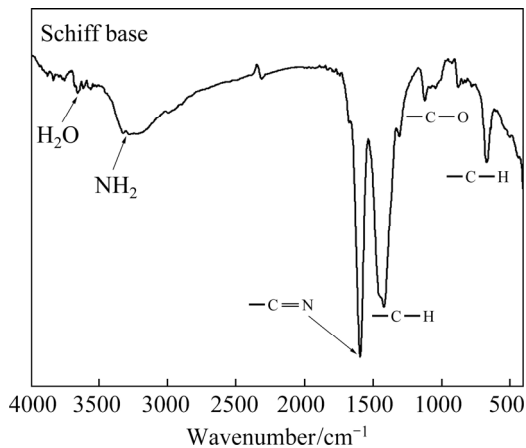
Fig. 2 FT-IR spectrum of Schiff base solution

3.2 Surface analysis of samples

The microstructures of the Ca−P and anodic Ca−P$_{Schiff\ base}$ coatings are shown in Fig. 3. The surface of all samples is covered by radial grains. However, the traditional Ca−P coating has an irregular grain shape with uneven distribution, and grain agglomeration phenomenon [25]; while anodic Ca−P$_{Schiff\ base}$ coating has a regular grain shape with

a uniform distribution. The element contents of the coatings are given in Table 1. As can be observed in Table 1, C, N, and S elements are detected in the anodic Ca−P$_{Schiff\ base}$ coating, indicating that Schiff base is incorporated into the coating. The Ca/P ratio of the traditional Ca−P coating at different locations is varied, which shows the formation of calcium phosphate crystals is uneven, whereas the Ca/P ratio of the anodic Ca−P$_{Schiff\ base}$ coating in different positions is similar, indicating that the distribution of calcium phosphate grains is very uniform.

Figure 4 shows the cross-sectional micro-structures of the coating and its element distribution. The anodic Ca−P$_{Schiff\ base}$ coating is smoother than Ca−P coating, i.e., the micro grain distribution of anodic Ca−P$_{Schiff\ base}$ coating is more uniform than that of Ca−P coating, which is consistent with the analysis results in Fig. 3. In addition, the thickness of anodic Ca−P$_{Schiff\ base}$ coating is (18.13±5.78) μm, about twice that of Ca−P coating (9.13±4.20) μm. The results show that the addition of Schiff base not only reduces the surface roughness of the coating but also increases the thickness of the coating,
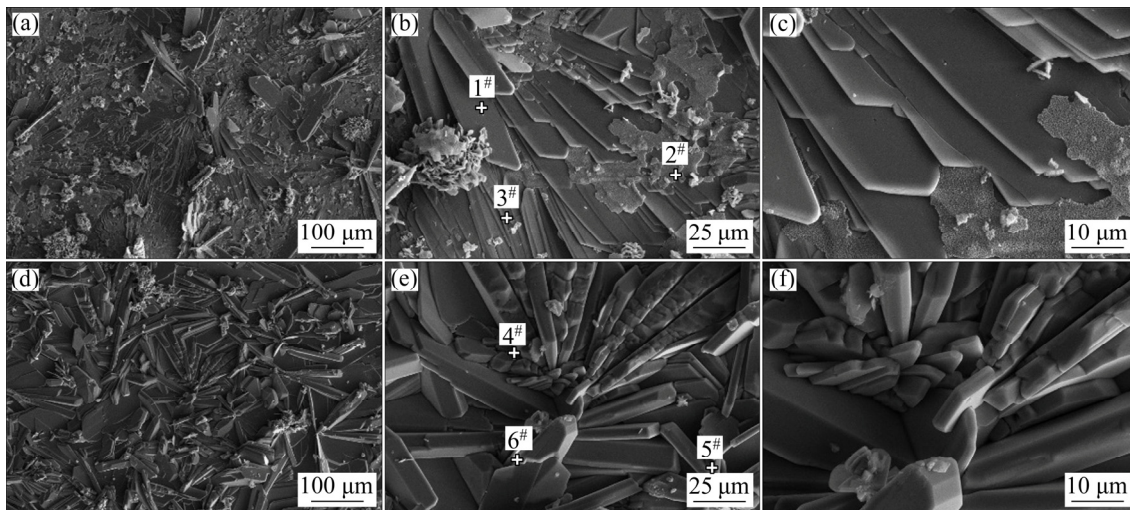

Fig. 3 SEM images of Ca−P (a−c) and anodic Ca−P$_{Schiff\ base}$ (d−f) coatings

Table 1 EDS analysis results of Ca−P and anodic Ca−P$_{Schiff\ base}$ coatings (at.%)

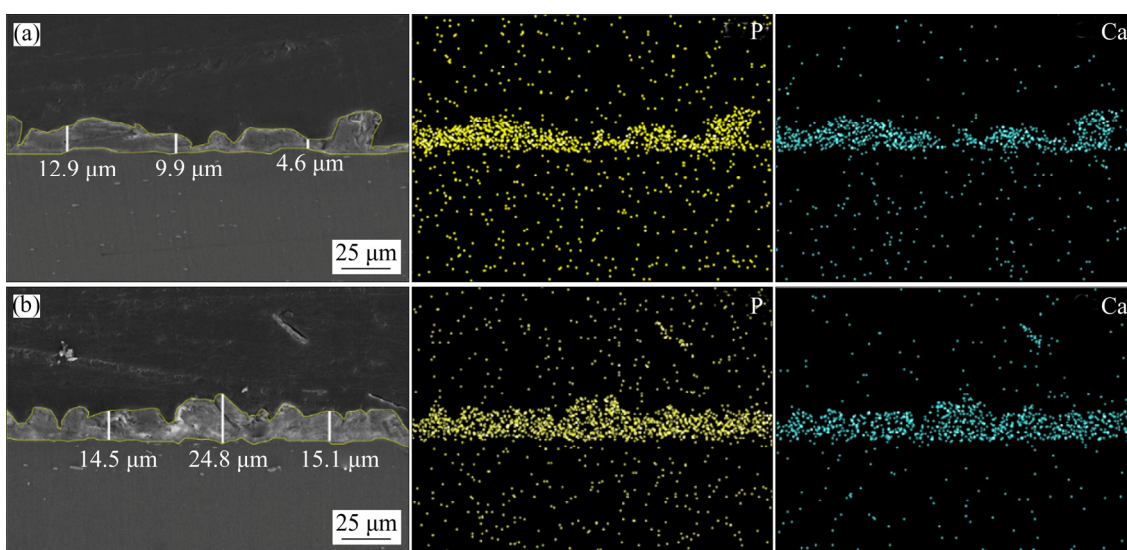| Point in Fig. 1	C	N	O	Mg	P	S	Ca	Ca/P
1	−	−	75.46	−	14.22	−	10.32	0.72
2	12.89	−	53.03	5.86	16.01	−	12.21	0.76
3	32.29	−	42.33	−	12.61	−	12.78	1.01
4	6.77	3.36	64.52	−	13.60	−	11.75	0.86
5	11.64	3.12	61.20	−	12.85	0.11	11.08	0.86
6	8.96	2.18	63.59	−	13.65	−	11.62	0.85

Fig. 4 Cross-sectional images and elemental mappings of Ca−P coating (a) and anodic Ca−P$_{Schiff\ base}$ coating (b)

which may be conducive to the improvement of the corrosion resistance.

To understand the effect of anodic Ca−P$_{Schiff\ base}$ coating on the surface morphology, 3D surface morphology analysis was performed. Figure 5 shows the mean surface roughness of Ca−P coating and anodic Ca−P$_{Schiff\ base}$ coating. As seen, the mean roughness (R_a) of Ca−P coating and Ca−P$_{Schiff\ base}$ coating is (1.76 ± 0.19) μm and (0.42 ± 0.08) μm, respectively. The Ca−P$_{Schiff\ base}$ coating is smoother than the Ca−P coating, showing that the addition of Schiff base reduces the roughness of the surface. The results suggest that the corrosion resistance of the coating is determined by the combination of surface morphology and thickness.

The chemical groups and crystallographic structures of the coatings were determined by FT-IR and XRD. The results are shown in Fig. 6. The characteristic peaks of PO_4^{3-} are found in Fig. 6(a), which mainly come from the calcium phosphate in the coating. XRD results show that α-Mg, CaHPO$_4$ (DCPA), and hydroxyapatite (HA) are found in anodic Ca−P$_{Schiff\ base}$ coating, but no HA in the Ca−P coating. It is known that HA is the main inorganic component of natural bone with excellent biological activity and biocompatibility [26]. Therefore, anodic Ca−P$_{Schiff\ base}$ coating is expected to have good bioactivity and biocompatibility.

The characteristic peak of Schiff base (—C=N) is not found in the detection of FT-IR spectra (Fig. 6(a)), which can be due to the small content of Schiff base. Therefore, in order to better determine the chemical compositions, anodic
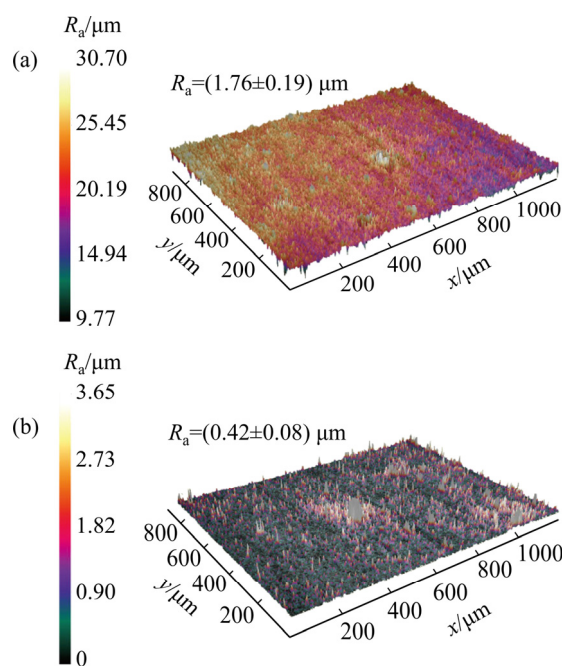

Fig. 5 Surface roughness of Ca−P coating (a) and anodic Ca−P$_{Schiff\ base}$ coating (b)

Ca−P$_{Schiff\ base}$ coating was analyzed using XPS. The results are shown in Fig. 7. Figure 7(a) shows the whole range of the binding energy survey on anodic Ca−P$_{Schiff\ base}$ coating. Obviously, the surface chemical compositions, in good agreement with the EDS results, contain Ca, P, C, N, S, and O elements. The elements of C, N, and S originate from the Schiff base. Figures 7(b−d) designate the curve fits of the C 1s, N 1s, and S 2p spectra of the anodic Ca−P$_{Schiff\ base}$ coating. The C 1s spectra can be split into four peaks. The C 1s signal at 285.6 eV can be attributed to hydrocarbon species (C—H/C—C) [16].
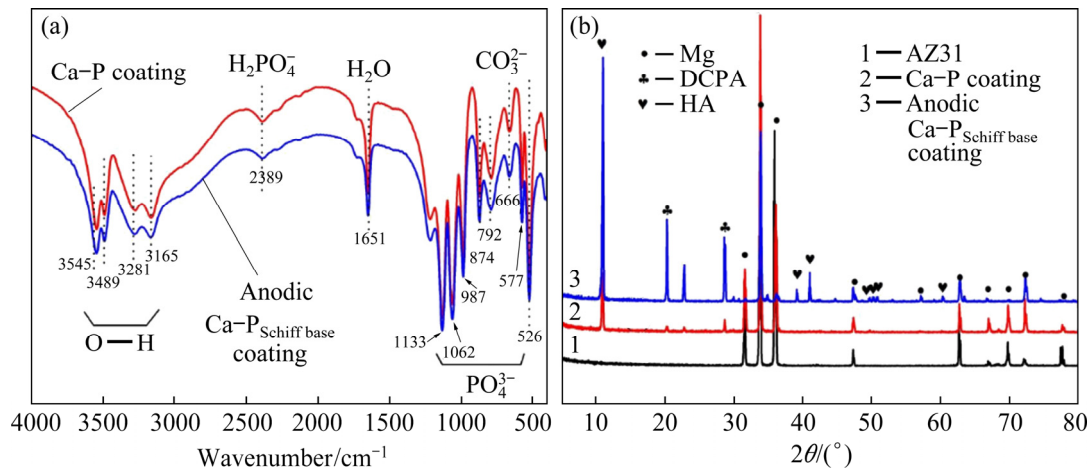
Fig. 6 FT-IR spectra (a) and XRD patterns (b) of AZ31 Mg alloy, Ca−P coating and anodic Ca−P$_{Schiff\,base}$ coating
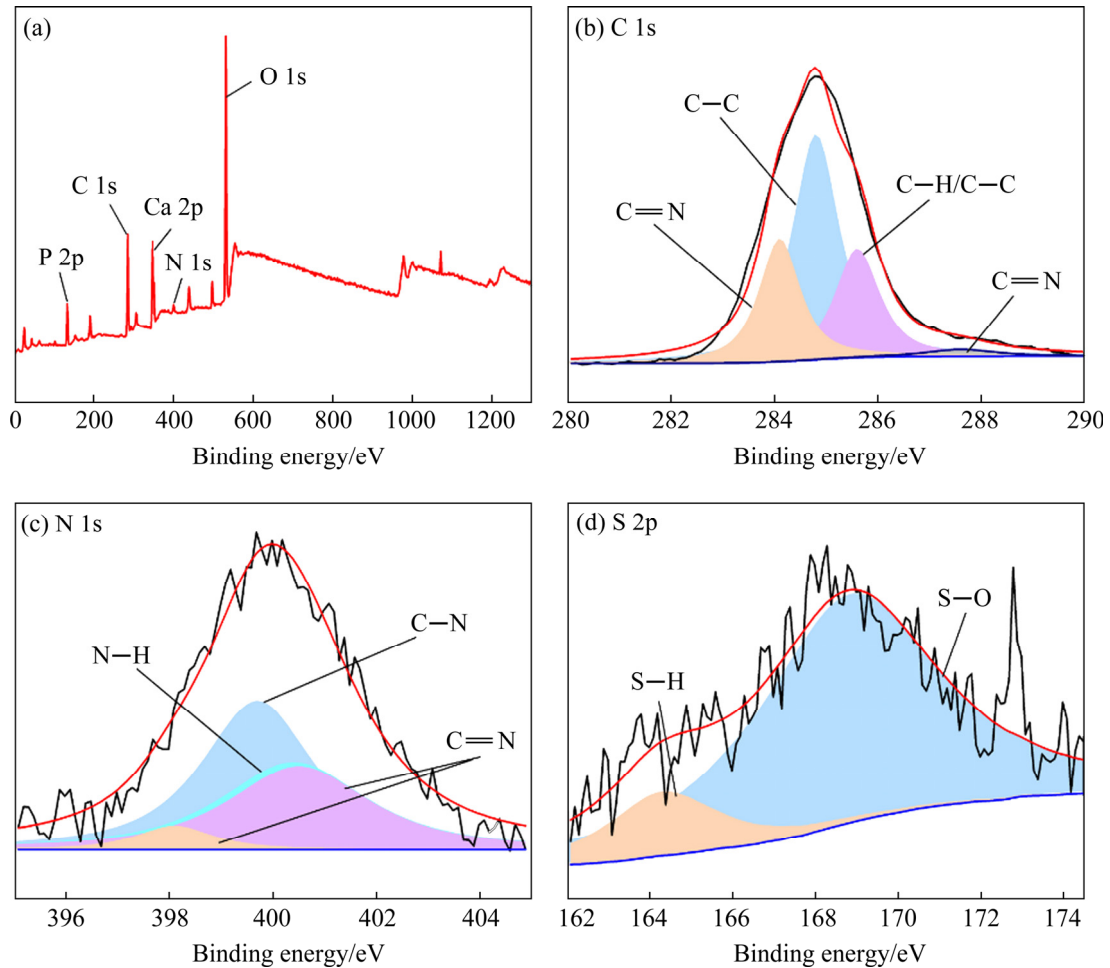

Fig. 7 XPS survey plot (a) and high-resolution spectra of C 1s (b), N 1s (c) and S 2p (d)

The other component at 284.8 eV may be related to the presence of C—C bonding, while the special peaks, at 287.5 eV and 284.1 eV, correspond to the C=N group [27]. According to the N 1s spectrum, N is derived from C—N (399.7 eV) and N—H (400.4 eV) in *L*-cysteine. In addition, the C=N characteristic peaks are observed at 400.5 and 398.1 eV [28]. The characteristic peak of C=N is found from the fine spectra of C and N elements, indicating that Schiff base participates in the

coating formation. The S 2p spectra are divided into two peaks, S—H at 164.3 and S—O at 168.9 eV [29], which may be due to the oxidation of the mercapto group.

The dependence of the applied load on the sliding distance after the nanoscratch tests is shown in Fig. 8. The load value of Ca−P coating ((3723±0.25) mN) is lower than that of anodic Ca−P$_{Schiff\,base}$ coating ((4988±0.25) mN), indicating a better adhesion between anodic Ca−P$_{Schiff\,base}$ coating and AZ31 substrate [30]. This also suggests that the Schiff base can improve the bond strength between the coating and the Mg alloy.
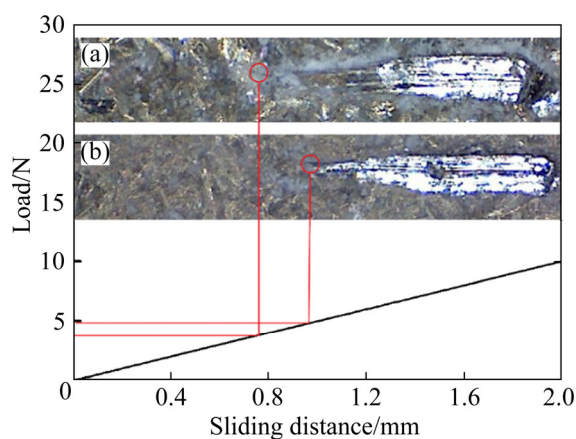

Fig. 8 Nanoscratch results of Ca−P coating (a) and anodic Ca−P$_{Schiff\,base}$ coating (b)

3.3 Corrosion behaviors

Figure 9 shows the OCP curves of the AZ31 Mg alloy, Ca−P coated alloy, and anodic Ca−P$_{Schiff\,base}$ coated alloy. When the potential difference between two different metal electrodes exceeds 50 mV, the risk of galvanic corrosion increases [31,32]. The OCP of Ca−P coated alloy is lower than that of the matrix at the beginning, increases gradually with the reaction, and exceeds that of the AZ31 Mg alloy after 1535 s. The OCP difference between the Ca−P coated alloy and the substrate keeps below 50 mV (vs SCE) during the reaction, which indicates that the Ca−P coating is mainly chemically dissolved at this time, while the possibility of galvanic corrosion is small [8,33,34]. For the anodic Ca−P$_{Schiff\,base}$ coated alloy, the OCP difference between the coated alloy and the substrate at the beginning of the reaction is 267 mV (vs SCE), indicating galvanic corrosion. With the reaction going on, a corrosion product layer is formed on the surface of the coating, which inhibits the galvanic corrosion, so the OCP difference between the coated alloy and the substrate decreases gradually [35,36].

The PDP curves of the AZ31 Mg alloy, Ca−P coated alloy, and anodic Ca−P$_{Schiff\,base}$ coated alloy are shown in Fig. 10. The fitting results of φ_{corr} and J_{corr} obtained by Tafel extrapolation are listed in Table 2. Generally, the lower the J_{corr} is, the better the corrosion resistance of the coating is. The values of J_{corr} are arranged from large to small in the following order: AZ31 Mg alloy (1.65× 10^{-5} A/cm^2) > Ca−P coating (5.53×10^{-6} A/cm^2) > anodic Ca−P$_{Schiff\,base}$ coating (6.61×10^{-7} A/cm^2), which shows that the anodic Ca−P$_{Schiff\,base}$ coated alloy has the best corrosion resistance. At the same time, the higher the breakdown potential (φ_b) is, the better the corrosion resistance of the coating is [37,38]. The R_p values are in the following order: AZ31 Mg alloy (2.21 kΩ·cm^2) < Ca−P coated alloy
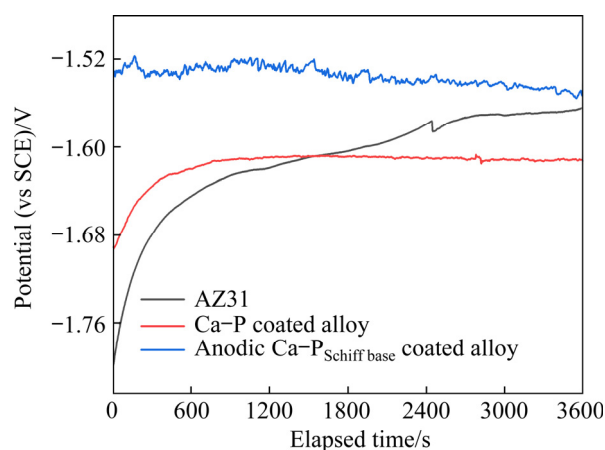

Fig. 9 OCP curves of AZ31 Mg alloy, Ca−P coated alloy and anodic Ca−P$_{Schiff\,base}$ coated alloy
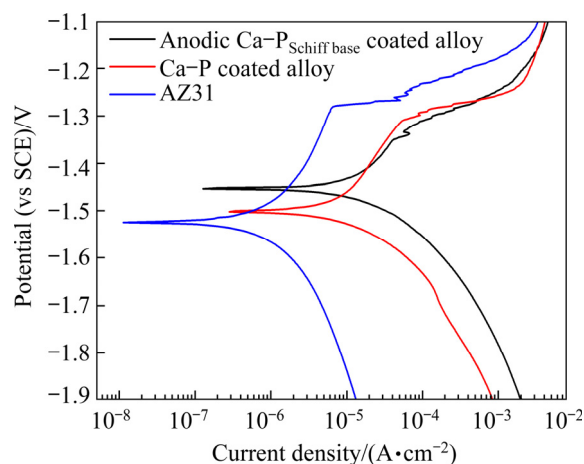
Fig. 10 PDP curves of AZ31 Mg alloy, Ca−P coated alloy and anodic Ca−P$_{Schiff\,base}$ coated alloy

(4.99 kΩ·cm²) < anodic Ca−P$_{Schiff base}$ coated alloy (58.31 kΩ·cm²). This further proves that anodic Ca−P$_{Schiff base}$ coating provides the best corrosion resistance to the alloy.

Nyquist and Bode plots of the AZ31 Mg alloy, Ca−P coated alloy, and anodic Ca−P$_{Schiff base}$ coated alloy are shown in Fig. 11. And the EIS results are analyzed by introducing the corresponding equivalent circuit model. In the equivalent circuits, R_s indicates solution resistance; CPE$_1$ and CPE$_2$ represent constant phase angle components; R_{ct} represents charge transfer resistance; R_L and L signify inductive resistance and inductance, respectively; R_1 means coating resistance [39,40]. Table 3 gives the specific fitting data. The Nyquist curves of AZ31 Mg alloy and Ca−P coated alloy are composed of medium- and high-frequency capacitor rings and low-frequency inductor rings. The medium and high-frequency capacitor rings are usually attributed to charge transfer (R_{ct}), while the low-frequency induction rings are represented by R_L and L, which are related to pitting and corrosion products or coating falling off from samples [41,42]. In addition, the appearance of the inductor in low-frequency implies the

occurrence of pitting [43−45]. From Table 3, the R_L (1218.00 Ω·cm²) of the Ca−P coated alloy is significantly larger than that of the AZ31 Mg alloy (230.50 Ω·cm²), indicating that the pitting of the Ca−P coating is more serious than that of the AZ31 Mg alloy. This is due to the thin and loose structure of Ca−P coating, which results in the corrosion medium easily reaching the substrate through the through-hole and causing corrosion. However, for anodic Ca−P$_{Schiff base}$ coating, there is no inductor in the low-frequency region, which indicates that anodic Ca−P$_{Schiff base}$ coating has a dense structure protecting the substrate from pitting. Moreover, the R_{ct} (23720.00 Ω·cm²) of anodic Ca−P$_{Schiff base}$ coating is about 41 times that of AZ31 Mg alloy (578.20 Ω·cm²) and five times that of Ca−P coating (4597.00 Ω·cm²). It is proven that the anodic Ca−P$_{Schiff base}$ coating has excellent corrosion resistance. In addition, the $|Z|_{0.01\,Hz}$ of anodic Ca−P$_{Schiff base}$ coating is the largest (Fig. 11(b)), which also proves that the corrosion resistance of anodic Ca−P$_{Schiff base}$ coating is the best.

The long-term corrosion resistance of the samples is evaluated by a hydrogen evolution test, and the results are shown in Fig. 12. In the early

Table 2 EIS analysis results of AZ31 Mg alloy, Ca−P coated alloy and anodic Ca−P$_{Schiff base}$ coated alloy

Sample	φ_{corr}(vs SCE)/V	J_{corr}/(A·cm^{-2})	β_a/(mV·dec^{-1})	$-\beta_c$/(mV·dec^{-1})	R_p/(kΩ·cm^2)
AZ31 Mg alloy	−1.45	1.65×10^{-5}	130.27	235.07	2.21
Ca−P coated alloy	−1.49	5.53×10^{-6}	118.19	137.58	4.99
Anodic Ca−P$_{Schiff base}$ coated alloy	−1.52	6.61×10^{-7}	203.23	157.51	58.31

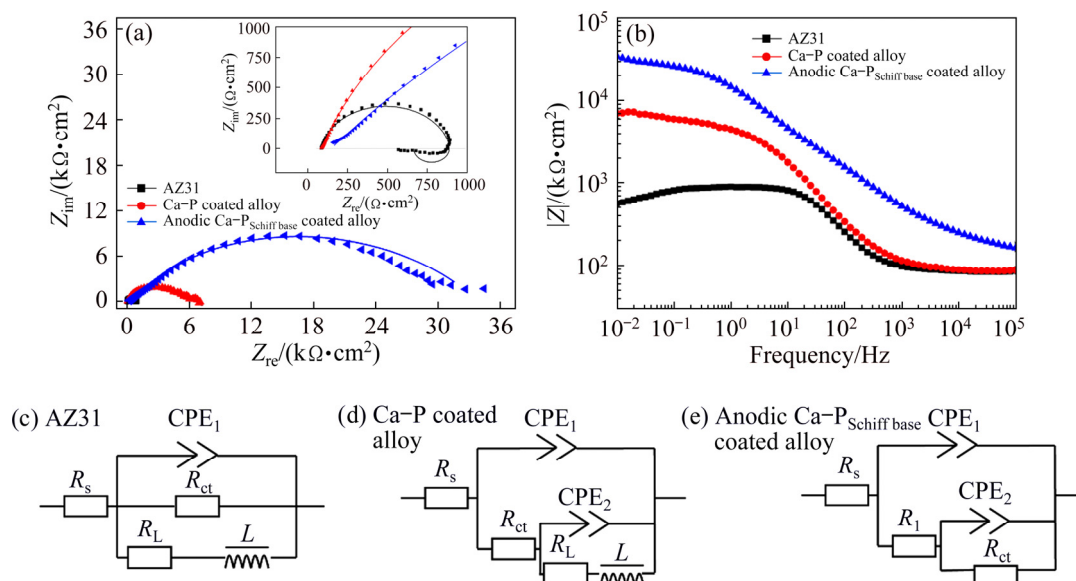**Fig. 11** Nyquist (a) and Bode (b) plots and equivalent circuits (c−e) of AZ31 Mg alloy, Ca−P coated alloy and anodic Ca−P$_{Schiff base}$ coated alloy

Table 3 EIS analysis results of AZ31 Mg alloy, Ca−P coated alloy and anodic Ca−P$_{\text{Schiff base}}$ coated alloy

Parameter	AZ31 Mg alloy	Ca−P coated alloy	Anodic Ca−P$_{\text{Schiff base}}$ coated alloy
$R_s/(\Omega\cdot\text{cm}^2)$	89.91	87.12	145.60
$\text{CPE}_1/$ $(\Omega^{-1}\cdot\text{s}^n\cdot\text{cm}^{-2})$	1.27×10^{-5}	1.73×10^{-5}	1.54×10^{-5}
n_1	0.91	0.81	0.57
$R_1/(\Omega\cdot\text{cm}^2)$	−	−	1.01×10^4
$\text{CPE}_2/$ $(\Omega^{-1}\cdot\text{s}^n\cdot\text{cm}^{-2})$	−	7.64×10^{-5}	1.53×10^{-4}
n_2	−	0.21	0.80
$R_{ct}/(\Omega\cdot\text{cm}^2)$	578.20	4579.00	23720.00
$L/(\text{H}\cdot\text{cm}^2)$	4.33×10^4	6.22×10^4	−
$R_L/(\Omega\cdot\text{cm}^2)$	230.50	1218.00	−
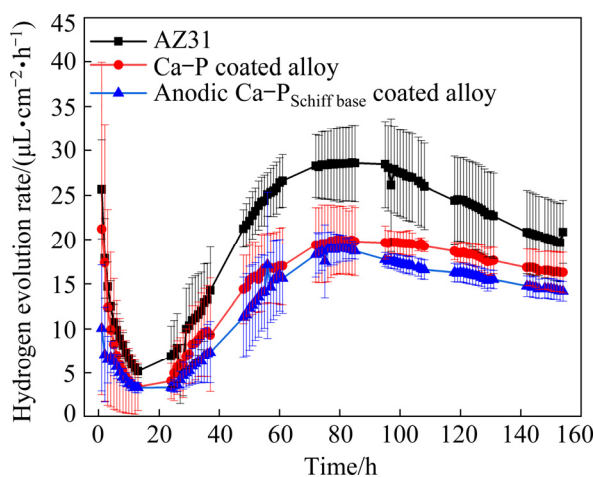
Fig. 12 Hydrogen evolution rates of AZ31 Mg alloy, Ca−P coated alloy and anodic Ca−P$_{\text{Schiff base}}$ coated alloy

stage of immersion, due to the formation of an oxide film or the existence of surface coating, the hydrogen evolution rate of the samples decreases rapidly. After 24 h of immersion, the hydrogen evolution rate gradually increases, which shows that the surface oxide film or coating is gradually damaged, resulting in the part substrate being exposed in the corrosive medium [41]. After nearly 80 h of immersion, the hydrogen evolution rate gradually decreases and tends to be stable. This shows that a corrosion product film is formed on the sample surface, which produces secondary protection. In the whole immersion process, the hydrogen evolution rate of the samples with coating protection is much lower than that of the AZ31 Mg

alloy substrate, especially for the samples with anodic Ca−P$_{\text{Schiff base}}$ coating. The results suggest that the anodic Ca−P$_{\text{Schiff base}}$ coating can provide the best protection for the substrate.

Figure 13 shows the macro- and micro-morphologies of the AZ31 Mg alloy, Ca−P coated alloy, and anodic Ca−P$_{\text{Schiff base}}$ coated alloy after 168 h immersion. The EDS results are given in Table 4. As can be observed from Fig. 13(a), the Mg alloy substrate is seriously corroded. From the SEM images (Figs. 13(d, c)) and Table 4, the substrate surface is full of cracks, with a small number of Ca−P products. However, for Ca−P coating or anodic Ca−P$_{\text{Schiff base}}$ coating, the radial Ca−P grains on the surface of the sample disappear. The Ca−P coating is locally corroded, i.e., part of the sample has an exposed substrate and is full of cracks (Figs. 13(e, f), while the other most areas are still covered by the coating and corrosion products (Figs. 13(g, h)). The anodic Ca−P$_{\text{Schiff base}}$ coating is intact with a few cracks (Figs. 13(i−k)), and the surface is full of Ca−P products. It is worth noting that N and S elements are not detected on the surface of anodic Ca−P$_{\text{Schiff base}}$ coating, which may be due to the Ca−P corrosion products covering the original coating or the less content of Schiff base in the coating itself.

The sample immersed for 168 h in Hank's solution was subjected to FT-IR and XRD analysis to determine the corrosion products. It can be seen from Fig. 14(a) that all the samples show a peak of —OH at 3483 cm^{-1}, indicating that the corrosion products of samples all contain Mg(OH)$_2$ [46−48]. The identical characteristic peaks at 872, 1426, and 1490 cm^{-1} indicate the formation of carbonates (Fig. 14(a)) on the surface due to the chemical reaction of Mg(OH)$_2$ with CO$_2$, which comes from air in the long immersion [49]. The results of FT-IR spectra show that the corrosion products of the conversion coating are mainly Mg(OH)$_2$ and trace MgCO$_3$. Comparing XRD patterns (Fig. 14(b)) of the coated samples and AZ31 Mg alloy substrate also confirms the presence of Mg(OH)$_2$ in the corrosion products. Furthermore, DCPA exists in the XRD pattern, which illustrates that the coating does not flake off and the sample is protected for a long time. However, there is no peak of MgCO$_3$ phase in the XRD pattern, indicating that the content of MgCO$_3$ is very small.
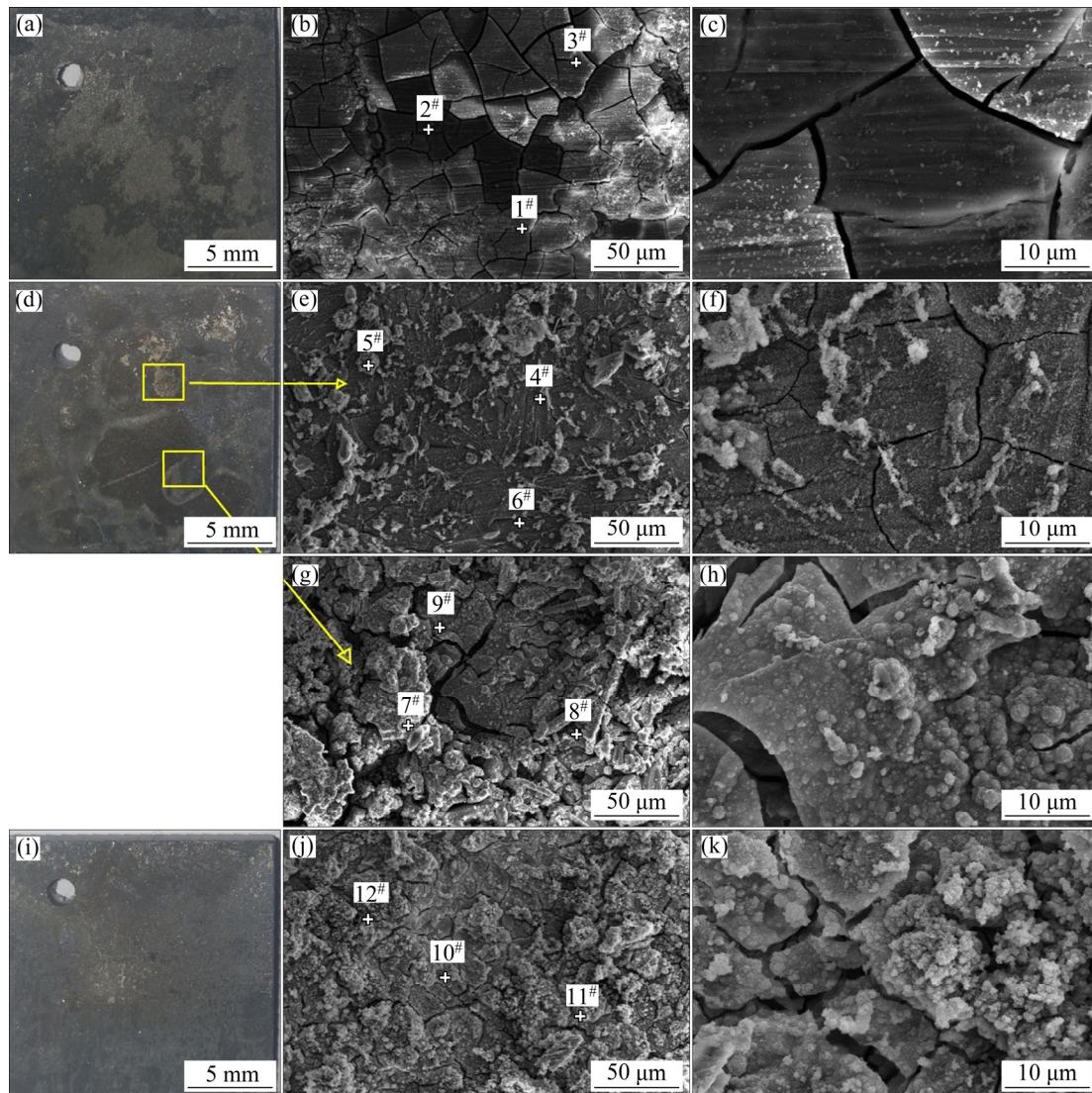
Fig. 13 Digital camera photographs (a, d, i) and SEM morphologies (b, c, e−h, j, k) for AZ31 Mg alloy (a−c), Ca−P coating (d−h) and anodic Ca−P$_{\text{Schiff base}}$ coating (i−k) after 168 h immersion

Table 4 EDS analysis results of samples after immersion for 168 h (at.%)

Point	C	O	Mg	Al	P	Ca	Ca/P
1	12.44	59.93	8.95	2.51	10.56	5.61	0.53
2	11.84	62.29	10.80	3.35	7.69	4.03	0.52
3	11.47	62.79	11.99	3.49	7.16	3.10	0.43
4	9.54	59.31	8.04	1.36	10.64	11.11	1.04
5	22.11	56.42	5.80	1.12	6.94	7.60	1.09
6	34.57	44.57	7.47	1.18	6.47	5.74	0.88
7	19.56	58.40	5.65	−	8.98	7.41	0.82
8	40.22	17.17	39.48	−	2.08	1.05	0.50
9	24.14	49.81	5.37	0.13	10.80	9.75	0.90
10	13.94	32.86	6.01	0.93	19.68	26.58	1.35
11	25.24	42.82	7.15	0.32	13.87	10.59	0.76
12	24.84	52.99	7.30	1.35	8.26	5.26	0.63

4 Discussion

4.1 Effect of organic additives

Ca−P coating has good biocompatibility because of its similar composition with bone tissue. The preparation of Ca−P coating on the surface of Mg alloy not only plays an important role in controlling and reducing the degradation rate but also improves biocompatibility [50]. However, the traditional Ca−P coating usually has many coarse grains and a large porosity, which leads to insufficient corrosion resistance and premature mechanical failure during the service life. This work shows that certain organic compounds can induce a better corrosion resistance to Ca−P coating without affecting the biocompatibility of the coating [51].
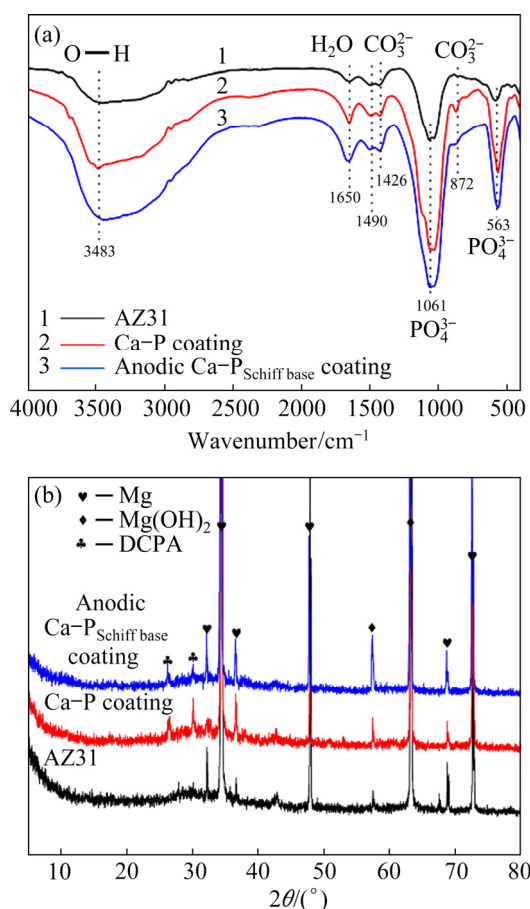
Fig. 14 FT-IR spectra (a) and XRD patterns (b) after 168 h immersion of AZ31 Mg alloy, Ca−P coating and anodic Ca−P$_{\text{Schiff base}}$ coating

GUO et al [46] developed a composite coating containing Ca−P and collagen (Col) on the Mg alloy and demonstrated that collagen-coated Mg alloy possesses higher implant stability and osseo-integration rate. The Ca−P$_{\text{Col}}$ coating indicated a protection efficiency superior to the Mg alloy substrate from the corrosion. The Ca−P$_{\text{Col}}$ coating in the presence of Col exhibited a smaller J_{corr} (8.70×10^{-7} A/cm^2) than Ca−P coating in the absence of Col (9.7×10^{-6} A/cm^2), with an increase in the R_{ct} value obviously from 1.40×10^4 to 1.10×10^5 Ω·cm^2, implying that the Ca−P$_{\text{Col}}$ coating can provide better protection for Mg alloy.

WANG et al [52] fabricated a super-hydrophobic needle-like Ca−P coating on AZ31 Mg alloy through modification with stearic acid (STA). The Ca−P$_{\text{STA}}$ coating with STA exhibited exceptional self-cleaning ability and mechano-chemical stability. The J_{corr} value of the super-hydrophobic needle-like Ca−P coated sample was 3.52×10^{-7} A/cm^2, which was more than two orders

of magnitude lower than that of the substrate (1.89×10^{-5} A/cm^2). The R_{ct} was 3.75×10^4 Ω·cm^2 for the superhydrophobic needle-like Ca−P coated sample and 1.62×10^3 Ω·cm^2 for the AZ31 substrate. It is clearly evident from the results that the Ca−P$_{\text{STA}}$ coating with needle-like structures contributed to the better corrosion resistant.

Recently, our group developed glucose induced Ca−P coating on the surface of pure Mg by hydrothermal method [16]. The coating was composed of block particles of different sizes. The coating induced by glucose was denser and more uniform than that without glucose. The composition of Ca−P coating induced by glucose was the same as that of the coating without glucose, which was composed of DCPA, HA, and CDHA (Ca$_{10-x}$(HPO$_4$)$_x$(PO$_4$)$_{6-x}$(OH)$_{2-x}$). It is worth noting that the presence of —COOH was detected by XPS, indicating that the transformation of glucose to gluconic acid occurred during the reaction. However, the R_{ct} of the Ca−P coating induced by glucose increased to three times that of the pure Mg substrate, and its J_{corr} (6.79×10^{-6} A/cm^2) was decreased by an order of magnitude compared with that of the pure Mg substrate (2.36×10^{-5} A/cm^2), as shown in Fig. 15. It is found that the conversion of glucose to gluconic acid can attract Ca^{2+} ions to the surface of Mg in the hydrothermal system, which can induce the formation of the Ca−P composite membrane and protect the bottom layer of Mg.

Amino acid induced Ca−P coating has also been prepared on AZ31 Mg alloy by low temperature water bath [17]. The coating was composed of radial Ca−P grains. The addition of amino acids significantly reduced the roughness of the coating and increased the thickness of the coating. By analyzing the composition of the coating, it was proven that the amino acid induced Ca−P coating contained only DCPA and CDHA, and did not contain HA. This may lead to the lower bone compatibility of amino acid induced Ca−P coating than that of glucose induced Ca−P coating. The J_{corr} of amino acid induced Ca−P coating (4.21×10^{-7} A/cm^2) was one order of magnitude lower than that of AZ31 Mg alloy (5.57×10^{-6} A/cm^2), and the R_{ct} was about 20 times higher than that of AZ31 Mg alloy (see Fig. 15). This was mainly due to the different forms of cysteine in the solution (depending on the pH value), in which the negatively charged functional

groups combine with Ca^{2+} and Mg^{2+} ions, while the positively charged functional groups attract anions in the solution. Therefore, it can capture the free metal ions in the solution, and increase the ion concentration at the substrate/solution interface, so as to promote the formation of the coating.
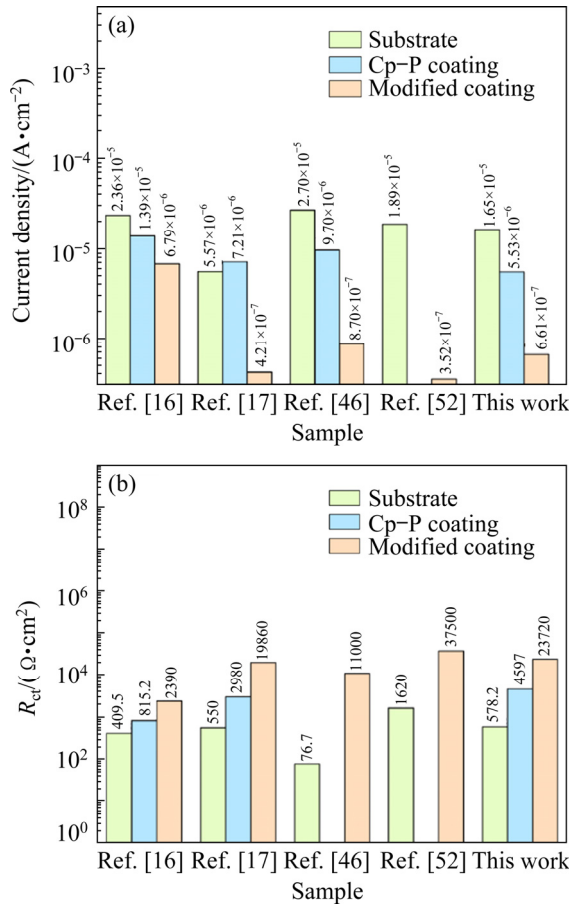

Fig. 15 Comparison of current density (a) and R_{ct} (b) of different modified coatings

In this work, Schiff base induced anodic Ca−P coating was prepared on the surface of AZ31 Mg alloy. Different from amino acid induced Ca−P coating, the crystallographic structures of anodic Ca−P$_{Schiff base}$ coating contain HA, while those without Schiff base only contain DCPA. Obviously, the Schiff base induces the formation of HA on the surface of Mg alloy. The anodic Ca−P$_{Schiff base}$ coating surface is composed of radial grains with uniform size, which shows that the addition of Schiff base can reduce porosity and coating non-uniformity caused by coarse grains [53]. From the electrochemical results, the J_{corr} of the anodic Ca−P$_{Schiff base}$ coating ($6.61×10^{-7}$ A/cm^2) is decreased by two orders of magnitude than that of the AZ31 Mg substrate ($1.65×10^{-5}$ A/cm^2). And after a long-term immersion test, the surface of the anodic Ca−P$_{Schiff base}$ coating shows little corrosion damage, which also proves that the Schiff base effectively maintains the corrosion resistance.

In summary, as can be seen from Fig. 15, the corrosion resistance of anodic Ca−P$_{Schiff base}$ ($J_{corr}=6.61×10^{-7}$ A/cm^2) is much better than that of glucose induced Ca−P coating ($J_{corr}=6.79×10^{-6}$ A/cm^2). And it is close to the corrosion resistance of collagen induced Ca−P coating ($J_{corr}=8.70×10^{-7}$ A/cm^2), amino acid induced Ca−P coating ($J_{corr}=4.21×10^{-7}$ A/cm^2), and stearic acid induced Ca−P coating ($J_{corr}=3.52×10^{-7}$ A/cm^2). As far as this study is concerned, glucose is converted into gluconic acid in solution, which contains —COOH group with strong polarity [54]. Meanwhile, cysteine contains —NH$_2$, —COOH, and —SH groups. Schiff base is prepared from glucose and cysteine. In addition to the above polar groups, the imino group is also formed. In terms of molecular structure, the complexation between Schiff base and metal ions is the strongest, and the corrosion resistance of calcium phosphate coating induced by Schiff base is the highest [55]. From the view of micro morphology, the crystal arrangement of the coating induced by the Schiff base is the most regular one. The preparation of anodic Ca−P$_{Schiff base}$ coating on the surface of Mg alloy not only plays an important role in controlling and reducing the degradation rate but also improves the biocompatibility. That is to say, the anodic Ca−P$_{Schiff base}$ coating has a better corrosion resistance than the glucose induced Ca−P coating, and also contains more HA crystallographic structures than the amino acid induced Ca−P coating.

4.2 Formation mechanism of Ca−P$_{Schiff base}$ coating

Based on the SEM, XRD, FTIR, and XPS analysis, the anodic Ca−P$_{Schiff base}$ coating formation mechanism is proposed. When the AZ31 Mg alloy is immersed in the solution of Ca−P conversion added with Schiff base, the dissolution of α-Mg occurs first [56,57] (Reaction 2). With the continuous diffusion of Mg^{2+} ions from the substrate/solution interface to the solution, they combine with the OH$^−$ in the conversion solution to form Mg(OH)$_2$ precipitation (Fig. 6(a)) (Reactions (3) and (4)). At the same time, Ca^{2+} ions in the

solution react with HPO_4^{2-} ions repeatedly in an alkaline environment (Reactions (5) and (6)), forming a calcium phosphorus product membrane composed of DCPA and HA (Fig. 6(b)). When supersaturation is reached, the product precipitates on the surface of the Mg alloy. In the whole process, the $-C=N$ groups in the molecular structure of Schiff base in solution is easy to complex with metal ions (containing Mg^{2+} and Ca^{2+} ions) [58,59], which can capture metal ions and stay at the solution/substrate interface, resulting in increasing the concentration of metal ions at the interface and promoting the precipitation reaction at the interface. In other words, the presence of the Schiff base promotes the formation of Ca−P precipitates. Figure 16 shows a schematic diagram of the formation mechanism of anodic Ca−P$_{Schiff base}$ coating.
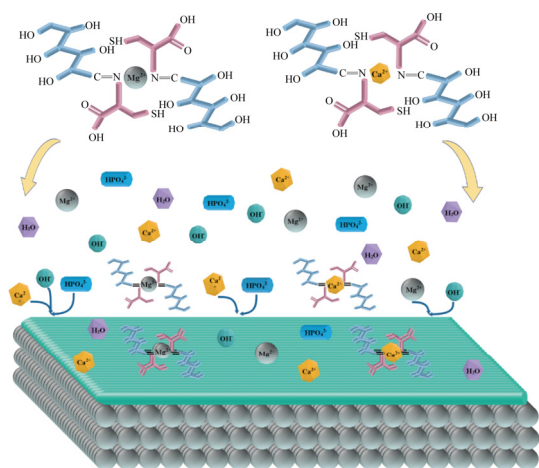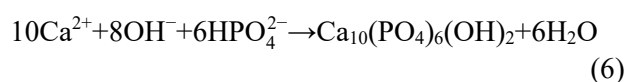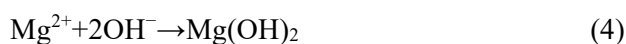
$$Mg \rightarrow Mg^{2+} + 2e \tag{2}$$

$$2H_2O + 2e \rightarrow H_2\uparrow + 2OH^- \tag{3}$$

$$Mg^{2+} + 2OH^- \rightarrow Mg(OH)_2 \tag{4}$$

$$Ca^{2+} + HPO_4^{2-} \rightarrow CaHPO_4 \tag{5}$$

$$10Ca^{2+} + 8OH^- + 6HPO_4^{2-} \rightarrow Ca_{10}(PO_4)_6(OH)_2 + 6H_2O \tag{6}$$

Fig. 16 Schematic diagram of formation mechanism of anodic Ca−P$_{Schiff base}$ coating

5 Conclusions

(1) The anodic Ca−P$_{Schiff base}$ coating refines the grains and has a dense microstructure. The mean roughness (R_a) of the Ca−P coating and anodic Ca−P$_{Schiff base}$ coating are (1.76±0.19) μm and (0.42±0.08) μm, respectively. The average thickness of the anodic Ca−P$_{Schiff base}$ coating is (18.13±

5.78) μm, nearly two times in comparison with that (9.13±4.20) μm of the Ca−P coating.

(2) The J_{corr} of anodic Ca−P$_{Schiff base}$ coating is one and two orders of magnitude lower than that of the Ca−P coating in the absence of Schiff base and AZ31 Mg alloy, respectively, indicating an improved corrosion resistance. The R_{ct} of anodic Ca−P$_{Schiff base}$ coating (23720.00 Ω·cm²) is over 40 times that of AZ31 Mg alloy (578.20 Ω·cm²). After a long time soaking test, the anodic Ca−P$_{Schiff base}$ coating is intact without any cracks, and also has the slowest hydrogen evolution rate. Thus, anodic Ca−P$_{Schiff base}$ coating has enhanced the corrosion resistance.

(3) The formation mechanism of anodic Ca−P$_{Schiff base}$ coating is proposed. Schiff base molecules and complexed metal ions in the ratio of 2:1, increase the saturation of the metal ions at substrate/solution interface, promote the forward process of a precipitation reaction, and accelerate the formation of the Ca−P precipitates.

References

[1] ACHESON J G, MCKILLOP S, LEMOINE P, BOYD A R, MEENAN B J. Control of magnesium alloy corrosion by bioactive calcium phosphate coating: Implications for resorbable orthopaedic implants [J]. Materialia, 2019, 6: 122360.

[2] YIN Zheng-zheng, QI Wei-chen, ZENG Rong-chang, CHEN Xiao-bo, GU Chang-dong, GUAN Shao-kang, ZHENG Yu-feng. Advances in coatings on biodegradable magnesium alloys [J]. Journal of Magnesium and Alloys, 2020, 8: 42−65.

[3] ZHANG Zhao-qi, YANG Yong-xin, LI Jian-an, ZENG Rong-chang, GUAN Shao-kang. Advances in coatings on magnesium alloys for cardiovascular stents—A review [J]. Bioactive Materials, 2021, 6: 4729−4757.

[4] FENG Li, ZHANG You-wei, WEN Chen, LI Si-zhen, LI Jia-feng, CHENG De, BAI Jing-ying, CUI Qing-xin. ZHANG Li-gong, Effect of initial deposition behavior on properties of electroless Ni−P coating on ZK60 and ME20 magnesium alloys [J]. Transactions of Nonferrous Metals Society of China, 2021, 31: 2307−2322.

[5] SU Ying-chao, GUO Yun-ting, HUANG Zi-long, ZHANG Zhi-hui, LI Guang-yu, LIAN Jian-she, REN Lu-quan.

Preparation and corrosion behaviors of calcium phosphate conversion coating on magnesium alloy [J]. Surface and Coatings Technology, 2016, 307: 99−108.

[6] LI Ling-yu, CUI Lan-yue, ZENG Rong-chang, LI Shuo-qi, CHEN Xiao-bo, ZHENG Yu-feng, KANNAN M B. Advances in functionalized polymer coatings on biodegradable magnesium alloys — A review [J]. Acta Biomaterialia, 2018, 79: 23−36.

[7] QIU Zai-meng, ZENG Rong-chang, ZHANG Fen, SONG Liang, LI Shuo-qi. Corrosion resistance of Mg−Al LDH/Mg(OH)₂/silane-Ce hybrid coating on magnesium alloy AZ31 [J]. Transactions of Nonferrous Metals Society of China, 2020, 30: 2967−2979.

[8] LIU Ping, WANG Jia-min, YU Xiao-tong, CHEN Xiao-bo, LI Shuo-qi, CHEN Dong-chu, GUAN Shao-kang, ZENG Rong-chang, CUI Lan-yue. Corrosion resistance of bioinspired DNA-induced Ca−P coating on biodegradable magnesium alloy [J]. Journal of Magnesium and Alloys, 2019, 7: 144−154.

[9] LIN Yi-shu, CAI Shu, JIANG Song, XIE Dong-li, LING Rui, SUN Jia-yue, WEI Jie-ling, SHEN Kaier, XU Guo-hua. Enhanced corrosion resistance and bonding strength of Mg substituted beta-tricalcium phosphate/Mg(OH)₂ composite coating on magnesium alloys via one-step hydrothermal method [J]. Journal of the Mechanical Behavior of Biomedical Materials, 2019, 90: 547−555.

[10] SONG Yang, ZHANG Shao-xiang, LI Jia-nan, ZHAO Chang-li, ZHANG Xiao-nong. Electrodeposition of Ca−P coatings on biodegradable Mg alloy: In vitro biomineralization behavior [J]. Acta Biomaterialia, 2010, 6: 1736−1742.

[11] ZHOU Wu-chao, HU Zhen-rong, WANG Tao-lei, YANG Guang-zheng, XI Wei-hong, GAN Yan-zi, LU Wei, HU Jing-zhou. Enhanced corrosion resistance and bioactivity of Mg alloy modified by Zn-doped nanowhisker hydroxyapatite coatings [J]. Colloids and Surfaces B: Biointerfaces, 2019, 186: 110710.

[12] LI Xia, WENG Zheng-yang, YUAN Wei, LUO Xian-zi, WONG H M, LIU Xiang-mei, WU Shui-lin, YEUNG K W K, ZHENG Yu-feng, CHU P K. Corrosion resistance of dicalcium phosphate dihydrate/poly(lactic-co-glycolic acid) hybrid coating on AZ31 magnesium alloy [J]. Corrosion Science, 2016, 102: 209−221.

[13] ZHANG Yuan-zhuang, MA Yu-chun, CHEN Min-fang, WEI Jun. Effects of anodizing biodegradable Mg−Zn−Zr alloy on the deposition of Ca−P coating [J]. Surface and Coatings Technology, 2013, 228: s111−s115.

[14] LI Chang-yang, FAN Xiao-li, ZENG Rong-chang, CUI Lan-yue, LI Shuo-qi, ZHANG Fen, HE Qing-kun, KANNAN M B, JIANG Hong-wei, CHEN Dong-chu, GUAN Shao-kang. Corrosion resistance of in-situ growth of nano-sized Mg(OH)₂ on micro-arc oxidized magnesium alloy AZ31—Influence of EDTA [J]. Journal of Materials Science and Technology, 2019, 35: 1088−1098.

[15] FAN Xiao-li, HUO Yuan-fang, LI Chang-yang, KANNAN M B, CHEN Xiao-bo, GUAN Shao-kang, ZENG Rong- chang, MA Quan-li. Corrosion resistance of nanostructured magnesium hydroxide coating on magnesium alloy AZ31: Influence of EDTA [J]. Rare Metals, 2019, 38: 520−531.

[16] LI Ling-yu, CUI Lan-yue, LIU Bin, ZENG Rong-chang, CHEN Xiao-bo, LI Shuo-qi, WANG Zhen-lin, HAN En-hou. Corrosion resistance of glucose-induced hydrothermal calcium phosphate coating on pure magnesium [J]. Applied Surface Science, 2019, 465: 1066−1077.

[17] FAN Xiao-li, LI Chang-yang, WANG Yu-bo, HUO Yuan-fang, LI Shuo-qi, ZENG Rong-chang. Corrosion resistance of an amino acid-bioinspired calcium phosphate coating on magnesium alloy AZ31 [J]. Journal of Materials Science and Technology, 2020, 49: 224−235.

[18] LIN Kai-dong, LUO Xiao-hu, PAN Xin-yu, ZHANG Cai-xia, LIU Ya-li. Enhanced corrosion resistance of LiAl-layered double hydroxide (LDH) coating modified with a Schiff base salt on aluminum alloy by one step in-situ synthesis at low temperature [J]. Applied Surface Science, 2019, 463: 1085−1096.

[19] da SILVA A B, D'ELIA E, da CUNHA PONCIANO GOMES J A. Carbon steel corrosion inhibition in hydrochloric acid solution using a reduced Schiff base of ethylenediamine [J]. Corrosion Science, 2010, 52: 788−793.

[20] BEHPOUR M, GHOREISHI S M, MOHAMMADI N, SOLTANI N, SALAVATI-NIASARI M. Investigation of some Schiff base compounds containing disulfide bond as HCl corrosion inhibitors for mild steel [J]. Corrosion Science, 2010, 52: 4046−4057.

[21] STANLY JACOB K, PARAMESWARAN G. Corrosion inhibition of mild steel in hydrochloric acid solution by Schiff base furoin thiosemicarbazone [J]. Corrosion Science, 2010, 52: 224−228.

[22] MO Shi, LI Ling-jie, LUO Hong-qun, LI Nian-bing. An example of green copper corrosion inhibitors derived from flavor and medicine: Vanillin and isoniazid [J]. Journal of Molecular Liquids, 2017, 242: 822−830.

[23] MA Liang, LI Wei-jie, ZHU Shi-jie, WANG Li-guo, GUAN Shao-kang. Corrosion inhibition of Schiff bases for Mg−Zn−Y−Nd alloy in normal saline: Experimental and theoretical investigations [J]. Corrosion Science, 2021, 184: 109268.

[24] WANG Yu, DING Bao-hua, GAO Shi-yu, CHEN Xiao-bo, ZENG Rong-chang, CUI Lan-yue, LI Shu-juan, LI Shuo-qi, ZOU Yu-hong, HAN En-hou, GUAN Shao-kang, LIU Qing-yun. In vitro corrosion of pure Mg in phosphate buffer solution—Influences of isoelectric point and molecular structure of amino acids [J]. Materials Science & Engineering C, 2019, 105: 110042.

[25] ALI A, IQBAL F, AHMAD A, IKRAM F, NAWAZ A, CHAUDHRY A A, SIDDIQI S A, REHMAN I. Hydrothermal deposition of high strength calcium phosphate coatings on magnesium alloy for biomedical applications [J]. Surface and Coatings Technology, 2019, 357: 716−727.

[26] TAYYABA Q, SHAHZAD M, ADNAN QAYUM B, RAFI UD D, KHAN M, QURESHI A H. The influence of electrophoretic deposition of HA on Mg−Zn−Zr alloy on its in-vitro degradation behaviour in the Ringer's solution [J]. Surface and Coatings Technology, 2019, 375: 197−204.

[27] AHAMAD T, NISHAT N. New antimicrobial epoxy-resin-bearing Schiff-base metal complexes [J]. Journal of Applied Polymer Science, 2008, 107: 2280−2288.

[28] WEI Zheng-wen, ZHANG Yao-yao, MA Xue-dong, WANG

Wei. Insight into the high-efficiency adsorption of pyrene by Schiff base porous polymers: Modelling and mechanism [J]. Polymer, 2021, 220: 123576.

[29] MAN Cheng, DONG Chao-fang, WANG Li, KONG De-cheng, LI Xiao-gang. Long-term corrosion kinetics and mechanism of magnesium alloy AZ31 exposed to a dry tropical desert environment [J]. Corrosion Science, 2020, 163: 108274.

[30] CUI Lan-yue, CHENG Shen-cong, LIANG Lu-xian, ZHANG Jjing-chao, LI Shuo-qi, WANG Zheng-lin, ZENG Rong-chang. In vitro corrosion resistance of layer-by-layer assembled polyacrylic acid multilayers induced Ca−P coating on magnesium alloy AZ31 [J]. Bioactive Materials, 2020, 5: 153−163.

[31] CUI Lan-yue, ZENG Rong-chang, GUAN Shao-kang, QI Wei-chen, ZHANG Fen, LI Shuo-qi, HAN En-hou. Degradation mechanism of micro-arc oxidation coatings on biodegradable Mg−Ca alloys: The influence of porosity [J]. Journal of Alloys and Compounds, 2017, 695: 2464−2476.

[32] ZHAO Yan-bin, LIU Han-peng, LI Chang-yang, CHEN Yong, LI Shuo-qi, ZENG Rong-chang, WANG Zhen-lin. Corrosion resistance and adhesion strength of a spin-assisted layer-by-layer assembled coating on AZ31 magnesium alloy [J]. Applied Surface Science, 2018, 434: 787−795.

[33] ZENG Rong-chang, HU Yan, GUAN Shao-kang, CUI Hong-zhi, HAN En-hou. Corrosion of magnesium alloy AZ31: The influence of bicarbonate, sulphate, hydrogen phosphate and dihydrogen phosphate ions in saline solution [J]. Corrosion Science, 2014, 86: 171−182.

[34] ZHANG Shan, CAO Fa-he, CHANG Lin-rong, ZHENG Jun-jun, ZHANG Zhao, ZHANG Jian-qing, CAO Chu-nan. Electrodeposition of high corrosion resistance Cu/Ni−P coating on AZ91D magnesium alloy [J]. Applied Surface Science, 2011, 257: 9213−9220.

[35] JAYARAJ J, RAJ S A, SRINIVASAN A, ANANTHAKUMAR S, PILLAI U T S, DHAIPULE N G K, MUDALI U K. Composite magnesium phosphate coatings for improved corrosion resistance of magnesium AZ31 alloy [J]. Corrosion Science, 2016, 113: 104−115.

[36] JIAN Shun-yi, CHU Yu-ren, LIN Chao-sung. Permanganate conversion coating on AZ31 magnesium alloys with enhanced corrosion resistance [J]. Corrosion Science, 2015, 93: 301−309.

[37] CUI Zhong-yu, LI Xiao-gang, XIAO Kui, DONG Chao-fang. Atmospheric corrosion of field-exposed AZ31 magnesium in a tropical marine environment [J]. Corrosion Science, 2013, 76: 243−256.

[38] LIU Qu, MA Qing-xian, CHEN Gao-qiang, CAO Xiong, ZHANG Shuai, PAN Ji-luan, ZHANG Gong, SHI Qing-yu. Enhanced corrosion resistance of AZ91 magnesium alloy through refinement and homogenization of surface microstructure by friction stir processing [J]. Corrosion Science, 2018, 138: 284−296.

[39] SHANAGHI A, MEHRJOU B, AHMADIAN Z, SOURI A R, CHU P K. Enhanced corrosion resistance, antibacterial properties, and biocompatibility by hierarchical hydroxyapatite/ciprofloxacin-calcium phosphate coating on nitrided NiTi alloy [J]. Materials Science and Engineering C, 2021, 118: 111524.

[40] WANG Zhi-hu, ZHANG Ju-mei, LI Yan, BAI Li-jing. ZHANG Guo-jun. Enhanced corrosion resistance of micro-arc oxidation coated magnesium alloy by superhydrophobic Mg−Al layered double hydroxide coating [J]. Transactions of Nonferrous Metals Society of China, 2019, 29: 2066−2077.

[41] LI Chang-yang, FAN Xiao-li, CUI Lan-yue, ZENG Rong-chang. Corrosion resistance and electrical conductivity of a nano ATO-doped MAO/methyltrimethoxysilane composite coating on magnesium alloy AZ31 [J]. Corrosion Science, 2020, 168: 108570.

[42] ZHANG Zhao-qi, WANG Li, ZENG Mei-qi, ZENG Rong-chang, LIN Cun-guo, WANG Zhen-lin, CHEN Dong-chu, ZHANG Qiang. Corrosion resistance and superhydrophobicity of one-step polypropylene coating on anodized AZ31 Mg alloy [J]. Journal of Magnesium and Alloys, 2021, 9: 1443−1457.

[43] KAABI FALAHIEH ASL S, NEMETH S, TAN M J. Improved corrosion protection of magnesium by hydrothermally deposited biodegradable calcium phosphate coating [J]. Materials Chemistry and Physics, 2015, 161: 185−193.

[44] KAVITHA R J, RAVICHANDRAN K, SANKARA NARAYANAN T S N. Deposition of strontium phosphate coatings on magnesium by hydrothermal treatment: Characteristics, corrosion resistance and bioactivity [J]. Journal of Alloys and Compounds, 2018, 745: 725−743.

[45] POKHAREL D B, WU Li-ping, DONG Jun-hua, WEI Xin, ETIM NABUK I I, SUBEDI D B, UMOH A J, KE Wei. Effect of D-fructose on the in-vitro corrosion behavior of AZ31 Magnesium alloy in simulated body fluid [J]. Journal of Materials Science & Technology, 2020, 66: 202−212.

[46] GUO Yun-ting, SU Ying-chao, GU Rui, ZHANG Zhi-hui, LI Guang-yu, LIAN Jian-she, REN Lu-quan. Enhanced corrosion resistance and biocompatibility of biodegradable magnesium alloy modified by calcium phosphate/collagen coating [J]. Surface and Coatings Technology, 2020, 401: 126318.

[47] ZENG Rong-chang, SUN Xin-xin, SONG Ying-wei, ZHANG Fen, LI Shuo-qi, CUI Hong-zhi, HAN En-hou. Influence of solution temperature on corrosion resistance of Zn−Ca phosphate conversion coating on biomedical Mg−Li−Ca alloys [J]. Transactions of Nonferrous Metals Society of China, 2013, 23: 3293−3299.

[48] ZENG Rong-chang, LIU Zhen-guo, ZHANG Fen, LI Shuo-qi, HE Qing-kun, CUI Hong-zhi, HAN En-hou. Corrosion resistance of in-situ Mg−Al hydrotalcite conversion film on AZ31 magnesium alloy by one-step formation [J]. Transactions of Nonferrous Metals Society of China, 2015, 25: 1917−1925.

[49] MAKKAR P, KANG H J, PADALHIN A R, FARUQ O, LEE B. In-vitro and in-vivo evaluation of strontium doped calcium phosphate coatings on biodegradable magnesium alloy for bone applications [J]. Applied Surface Science, 2020, 510: 145333.

[50] ZHANG Chun-yan, ZHANG Jun, ZHANG Shi-yu, WANG Zhen-lin. Comparison of calcium phosphate coatings on AZ31 and fluoride-treated AZ31 alloy prepared by hydrothermal method and their electrochemical corrosion

behaviour [J]. Materials Chemistry and Physics, 2018, 220: 395−401.

[51] HIROMOTO S. Self-healing property of hydroxyapatite and octacalcium phosphate coatings on pure magnesium and magnesium alloy [J]. Corrosion Science, 2015, 100: 284−294.

[52] WANG Li-yuan, XIAO Xi-mei, LIU En-yang, YU Si-rong, YIN Xiao-li, WANG Jun, ZHU Guang, LI Quan. LI Jing. Fabrication of superhydrophobic needle-like Ca−P coating with anti-fouling and anti-corrosion properties on AZ31 magnesium alloy [J]. Colloids and Surfaces A: Physicochemical and Engineering Aspects, 2021, 620: 126568.

[53] KAVITHA A, EASWARAMOORTHY D, THANGEESWARI T, PARTHIPAN G, SHANMUGAN S, ANSARI T. Synthesis and characterization of tritendate Schiff base rare earth nano metal complexes [J]. Materials Today: Proceedings, 2021, 34: 453−459.

[54] YAN Wei, LIAN Yi-jie., ZHANG Zhi-yuan, ZENG Mei-qi, ZHA Zhao-qi, YIN Zheng-zheng, CUI Lan-yue, ZENG Rong-chang. In vitro degradation of pure magnesium—The synergetic influences of glucose and albumin [J]. Bioactive Materials, 2020, 5: 318−333

[55] SHTAIWI M H, TAHBOUB D M, EL-SHEIKH A H, AL-HASHIMI N N. Magnetic solid-phase extraction of metal ions: Comparison of adding Schiff base to the extraction medium vs. magnetite modification with Schiff base [J]. Journal of Environmental Chemical Engineering, 2020, 8: 103675.

[56] EL-TAIB HEAKAL F, SHEHATA O S, TANTAWY N S. Enhanced corrosion resistance of magnesium alloy AM60 by cerium(III) in chloride solution [J]. Corrosion Science, 2012, 56: 86−95.

[57] ZENG Rong-chang, HU Yan, ZHANG Fen, HUANG Yuan-ding, WANG Zhen-lin, LI Shuo-qi, HAN En-hou. Corrosion resistance of cerium-doped zinc calcium phosphate chemical conversion coatings on AZ31 magnesium alloy [J]. Transactions of Nonferrous Metals Society of China, 2016, 26: 472−483.

[58] MENAKA R, GEETHANJALI R, SUBHASHINI S. Electrochemical investigation of eco-friendly chitosan Schiff base for corrosion inhibition of mild steel in acid medium [J]. Materials Today: Proceedings, 2018, 5: 16617−16625.

[59] LIANG Chu-xin, LIU Zheng, LIANG Qiu-qun, HAN Guo-cheng, HAN Jia-xing, ZHANG Shu-fen. FENG Xiao-zhen. Synthesis of 2-aminofluorene bis-Schiff base and corrosion inhibition performance for carbon steel in HCl [J]. Journal of Molecular Liquids, 2019, 277: 330−340.

AZ31 镁合金表面葡萄糖和 *L*-半胱氨酸仿生
席夫碱阳极钙磷涂层的耐腐蚀性能

王雪梅[1]，樊晓丽[1]，曾美琪[1]，李长阳[1]，崔蓝月[1]，陈晓博[2]，邹玉红[3]，王振林[4]，曾荣昌[1,5]

1. 山东科技大学 材料科学与工程学院 轻金属腐蚀实验室，青岛 266590；

2. School of Engineering, RMIT University, Carlton 3053, VIC, Australia；

3. 山东科技大学 化学与生物工程学院，青岛 266590；

4. 重庆理工大学 材料科学与工程学院，重庆 400054；

5. 郑州大学 材料科学与工程学院，郑州 450002

摘 要：通过往 60 ℃传统钙磷处理液中添加适量的氨基酸型席夫碱，在镁合金表面于 $CaCl_2$ 和 KH_2PO_4 混合溶液中制备席夫碱(含 C═N 的化合物)诱导的阳极 Ca−P 涂层。采用 FE-SEM、FT-IR、XRD 和 XPS 技术研究涂层的显微组织和化学成分，涂层试样的耐腐蚀性能则通过动电位极化(PDP)、电化学阻抗光谱(EIS)和析氢试验表征。结果表明，Ca−P$_{\text{Schiff base}}$ 涂层中存在 $CaHPO_4$(DCPA)和羟基磷灰石(HA)，而 Ca−P 涂层中没有 HA。此外，Ca−P$_{\text{Schiff base}}$ 涂层厚度(18.13±5.78) μm 大约为 Ca−P 涂层厚度(9.13±4.20) μm 的 2 倍。电化学结果表明，Ca−P$_{\text{Schiff base}}$ 涂层的腐蚀电流密度比 Ca−P 涂层降低两个数量级。最后，提出席夫碱作用下 Ca−P 涂层的形成机理。

关键词：镁合金；阳极涂层；耐蚀性；席夫碱；生物材料

(Edited by Bing YANG)